Phonon scattering in strained transition layers for GaN heteroepitaxy

Jungwan Cho,[1,*] Yiyang Li,[2] William E. Hoke,[3] David H. Altman,[3] Mehdi Asheghi,[1] and Kenneth E. Goodson[1,†]
[1]*Department of Mechanical Engineering, Stanford University, Stanford, California 94305, USA*
[2]*Department of Materials Science and Engineering, Stanford University, Stanford, California 94305, USA*
[3]*Raytheon Company, Andover, Massachusetts 02451, USA*
(Received 22 January 2013; revised manuscript received 27 January 2014; published 3 March 2014)

Strained transition layers, which are common for heteroepitaxial growth of functional semiconductors on foreign substrates, include high defect densities that impair heat conduction. Here, we measure the thermal resistances of AlN transition layers for GaN on Si and SiC substrates in the temperature range $300 < T < 550$ K using time-domain thermoreflectance. We propose a model for the effective resistance of such transition films, which accounts for the coupled effects of phonon scattering on defects and the two interfaces. The data are consistent with this model using point defects at concentrations near 10^{20} cm^{-3} and transmission coefficients based on the diffuse mismatch model. The data can be also described using lower transmission coefficients and eliminating the defects in the AlN. The data and modeling support the hypothesis that point defect scattering in the AlN film dominates the resistance, but may also be consistent with a high presence of near-interfacial defects in the bounding films.

DOI: 10.1103/PhysRevB.89.115301 PACS number(s): 72.10.Di, 63.22.Np, 65.40.−b, 68.35.−p

I. INTRODUCTION

Heteroepitaxial growth enables functional semiconducting devices to be fabricated from materials that may not be readily available in bulk form. One example is GaN grown on Si or SiC for laser diodes, light-emitting diodes, and high-electron mobility transistors [1–3]. Heteroepitaxy of GaN is generally achieved with a strained AlN transition layer to relieve stress due to the large lattice mismatch (3.5 and 17.0% for GaN-SiC and GaN-Si, respectively) and differing thermal expansion coefficients [4]. These transition films can be highly defective, and this can substantially impair heat conduction from the active GaN regions into the bulk substrate. Electron micrographs of GaN/AlN/SiC composites have shown high densities of dislocations on the order of 10^8–10^9 cm^{-2} in the GaN and 10^{10}–10^{12} cm^{-2} in the AlN [5–8]. Reitmeier *et al*. [5] suggested that the initial AlN layers on the growth substrate are nonstoichiometric and thus contain a very high density of point defects, which leads to a high density of dislocations in the near-interfacial volume of the epitaxial layer. Another electron micrograph investigation [9] of GaN/AlN/SiC composites compared defects in epitaxial heterostructures prepared using metal-organic chemical vapor deposition (MOCVD) and hydride vapor phase epitaxy (HVPE). This past work revealed that the MOCVD-grown sample was devoid of planar defects, whereas the HVPE-grown sample contained high densities of stacking faults in both GaN and AlN layers.

The past literature is far from conclusive on the magnitude, temperature dependence, and governing physics for the thermal resistance for conduction from the GaN into foreign substrates, especially for the thermal resistance of the strained AlN transition layer. The resistance mechanisms might include (a) phonon scattering at the AlN layer boundaries, (b) scattering on point defects, dislocations, and other disorders within the AlN, and (c) scattering by disorder in the GaN and the growth substrate within nanometers of the interface with the AlN. These mechanisms are nearly impossible to separate experimentally and can also be coupled in a quasiballistic phonon transport study [10–12]. We can, however, attempt to discern the dominant physics, and, for this purpose, the temperature dependence of the resistance can be informative. Discrete interface resistances generally decrease with increasing temperature owing to the increasing phonon heat capacity [13–15]. However, phonon scattering on lattice imperfections could result in the opposite temperature trend due to the strong frequency dependence of phonon scattering [16]. Micro-Raman thermometry on GaN device structures has suggested that the effective AlN thermal resistance may increase dramatically with temperature [17,18]. Our recent data [19] indicate that the resistance may be much lower for GaN/AlN/SiC than was found in these Raman studies and that imperfections may dominate over discrete traditional acoustic mismatch resistances at the AlN interfaces with the adjacent GaN and growth substrate. There remains an urgent need for a detailed temperature-dependent study for both GaN/AlN/SiC and GaN/AlN/Si composites that attempts to identify the types and concentrations of defects that are responsible for the resistance.

Here, we report the effective thermal resistance of the AlN transition layer $R_{\mathrm{AlN,eff}}$ as well as the thermal conductivity of the GaN overlayer k_{GaN} for GaN/AlN/SiC and GaN/AlN/Si composites. The data are obtained over the temperature range 300–550 K using time-domain thermoreflectance (TDTR). We use GaN thicknesses of 0.6, 0.9, and 1.6 μm and of 0.5, 1.3, and 1.7 μm, for GaN/AlN/SiC and GaN/AlN/Si, respectively, which aids with the extraction of the discrete AlN resistance in both cases. We employ an approximate solution to the phonon Boltzmann transport equation to further investigate effects of phonon scattering by microstructural defects on the measured temperature-dependent properties. While the AlN volume resistance and the boundary resistances at the AlN interfaces (GaN/AlN and AlN/SiC or AlN/Si) are not separable and are lumped into an effective AlN resistance, our analysis suggests that phonon scattering due to point defects can be particularly

*Corresponding author: jungwan.cho@stanford.edu
†goodson@stanford.edu

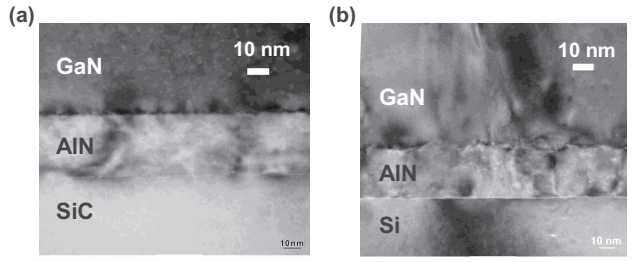

FIG. 1. Representative cross-sectional transmission electron micrographs near the GaN-substrate interfaces of (a) GaN/AlN/SiC and (b) GaN/AlN/Si. Approximately 57- and 60-nm layers of Al are evaporated on these GaN/AlN/SiC and GaN/AlN/Si structures, respectively, for optical thermoreflectance measurements.

important for the thermal resistance for conduction from the GaN to the growth substrate through the AlN layer.

II. EXPERIMENTAL DETAILS

A. Sample preparation

Figure 1 shows representative cross-sectional transmission electron micrographs near the GaN-substrate interfaces of both types of samples. We use three different thicknesses of GaN for both types of samples to vary the sensitivity of the measurement to the GaN thermal conductivity and to the effective AlN thermal resistance. For the GaN/AlN/SiC composites, the GaN epilayers are grown on 4H-SiC substrates by using standard MOCVD. The GaN layers are then etched to the three different thicknesses (0.6, 0.9, and 1.6 μm). As is typical for GaN on SiC materials, the AlN transition layer is very thin ($\sim$36 nm), as indicated in Fig. 1(a). The GaN/AlN/Si composite materials are grown by molecular beam epitaxy (MBE), followed by etching to the three different GaN thicknesses (0.5, 1.3, and 1.7 μm). The MBE growth of the GaN/AlN/Si composites enables the use of a very thin AlN transition layer [$\sim$38 nm; see Fig. 1(b)]. Typical MOCVD GaN-Si material has ternary transition layers that are approximately an order of magnitude thicker and exhibit lower thermal conductivity [18,20]. Evaporated Al layers of 57 and 60 nm serve as the metal transducers for thermoreflectance measurements on the GaN/AlN/SiC and GaN/AlN/Si composites, respectively.

B. Time-domain thermoreflectance

TDTR is a well-established technique for determining thermal conductivities and interface resistances in multilayer thin-film structures for a wide range of temperatures [21–27]. This approach uses brief heating pulses to confine the thermal penetration depth to the near-surface region, such that the measured thermal decay is sensitive to the targeted effective AlN resistance. In our setup, a mode-locked Nd:YVO_4 laser generates 9.2-ps optical pulses at 1064-nm wavelength and with 82-MHz repetition rate, which are divided into pump (as a heat source) and probe (as a thermometer) components. The frequency-doubled pump beam, modulated at 2 MHz by an electro-optic modulator for lock-in detection, heats the metal transducer. The surface temperature of the metal film is then monitored with the time-delayed probe beam via the changes in reflectivity of metal with temperature, i.e., the thermoreflectance. This temporal surface temperature response is related to the thermophysical properties of the sample of interest beneath the metal transducer.

From the output of the rf lock-in amplifier, which has an in-phase $V_{in}(t)$ and an out-of-phase $V_{out}(t)$ component, we monitor the amplitude $\sqrt{{V_{in}}^2 + {V_{out}}^2}$ of the thermoreflectance signal over the full range of delay time, $-0.1 \leqslant t \leqslant 3.6$ ns. The amplitude signal is compared to a three-dimensional radial symmetric solution of the heat equation for the multilayer stack taking into account modulated optical heating [22]. We use a single-mode fiber after the delay stage to address the problems caused by (a) enlargement of the probe spot size due to beam divergence and (b) displacement of the probe spot on the sample due to beam steering effects as the probe beam traverses the delay stage [21,26]. The divergence/steering-related enlargement/displacement of the probe spot is converted into a varying amplitude signal but with constant mode profile and constant position on the sample. The pump beam amplitude and the delay-time-dependent amplitude of the probe beam are monitored independently from the thermoreflected probe amplitude to correct for intensity fluctuations and for the intensity dependence on the stage position [26]. We validate system accuracy by extracting a thermal conductivity of 1.33 W m^{-1} K^{-1} and 145 W m^{-1} K^{-1} at room temperature for a thermally grown SiO_2 calibration sample and an intrinsic single-crystalline Si calibration sample, respectively, each of which is within 2% of the reference literature values for these materials [28–30]. By using a vacuum stage with optical access, we extend the TDTR measurements to temperatures up to 550 K. Further details of our TDTR setup are described in Ref. [26].

Both the amplitude $\sqrt{{V_{in}}^2 + {V_{out}}^2}$ and the ratio $-V_{in}/V_{out}$ of the in-phase and out-of-phase signals of the rf lock-in amplifier provide information from which the GaN thermal conductivity k_{GaN} and the effective AlN thermal resistance $R_{AlN,eff}$ can be extracted for the GaN composites studied here. Our analysis of the TDTR sensitivity indicates that both approaches provide comparable values of the sensitivity to k_{GaN} and $R_{AlN,eff}$ at our pump modulation frequency of 2 MHz. Although we discuss more details of the measurement sensitivity in the next section, describing quantitative sensitivity values here for both amplitude and ratio approaches will be useful for the comparison. For the thickest GaN/AlN/SiC, the absolute values of the sensitivity to k_{GaN} over the positive delay times (from 0 to 3.5 ns) are between 0.37 and 0.55 for the amplitude approach and between 0.38 and 0.64 for the ratio approach. For the thinnest GaN/AlN/SiC, the absolute values of the sensitivity to $R_{AlN,eff}$ over the positive delay times are between 0.19 and 0.23 and between 0.17 and 0.27 for the amplitude and ratio approaches, respectively.

Although both approaches offer comparable sensitivities to the properties examined, the amplitude approach has some advantages over the ratio approach for this specific set of samples. First, the amplitude signal is less sensitive to the substrate (SiC and Si) thermal conductivity than the ratio signal is. This is advantageous for the SiC-based samples, as the error propagated by uncertainties in the thermal conductivity

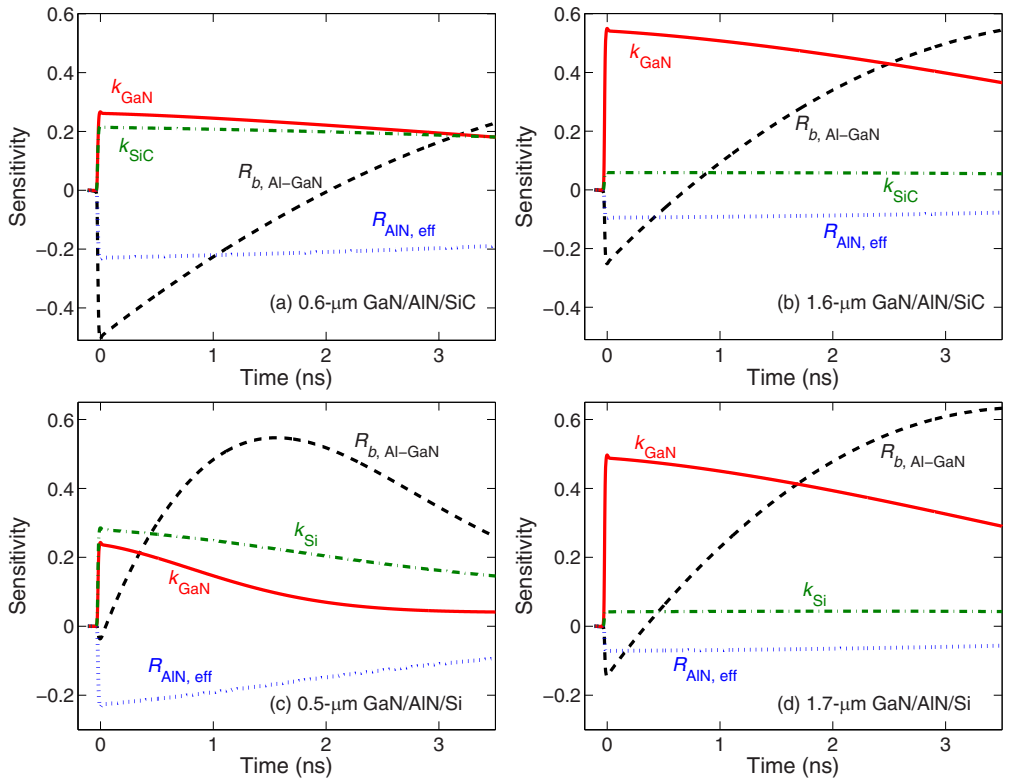

FIG. 2. (Color online) Sensitivity S_{α}, calculated by Eq. (1), to changes in four parameters in the thermal model as a function of delay time for the (a) 0.6 μm and (b) 1.6 μm GaN/AlN/SiC composites and the (c) 0.5 μm and (d) 1.7 μm GaN/AlN/Si composites at room temperature. Sensitivity values are evaluated at 2-MHz pump modulation frequency. Black dashed lines represent the sensitivity to the thermal boundary resistance at the Al/GaN boundary $R_{b,\text{Al-GaN}}$, red solid lines represent the sensitivity to the GaN thermal conductivity k_{GaN}, blue dotted lines represent the sensitivity to the effective AlN thermal resistance $R_{\text{AlN,eff}}$, and green dashed-dotted lines represent the sensitivity to the substrate thermal conductivity k_{SiC} or k_{Si}.

of the substrate is reduced. Our analysis for the thinnest GaN/AlN/SiC at room temperature finds that the absolute values of the sensitivity to k_{SiC} are slightly lower than those to $R_{\text{AlN,eff}}$ in the amplitude approach, whereas in the ratio approach the absolute values of the sensitivity to k_{SiC} are higher by a factor of two than those to $R_{\text{AlN,eff}}$. Second, the amplitude approach is free of error propagation associated with the uncertainty in setting the correct reference phase of the rf lock-in amplifier, whereas in the ratio approach, this uncertainty is one of the major sources of the total uncertainty, especially for a low-frequency measurement [25]. Since we use a relatively low modulation frequency of 2 MHz to probe the buried GaN-substrate thermal interface, the amplitude approach is beneficial for extracting the thermal resistance of this buried interface with lower uncertainty.

C. Sensitivity analysis

Measurements using TDTR extract the effective AlN thermal resistance $R_{\text{AlN,eff}}$ and the intrinsic GaN thermal conductivity k_{GaN}, as well as the Al/GaN thermal boundary resistance $R_{b,\text{Al-GaN}}$. We are grouping the AlN volume resistance and the AlN/GaN and AlN/SiC (or AlN/Si) boundary resistances into a single effective resistance $R_{\text{AlN,eff}}$ associated with the AlN film; therefore, what is actually reported here is the sum of the boundary and internal resistances. All the other input parameters in the multilayer thermal model are either measured independently or taken from the literature, including the thickness d_{Al}, thermal conductivity k_{Al}, and heat capacity C_{Al} of the Al transducer, the thickness d_{GaN} and heat capacity C_{GaN} of the GaN layer, and the thermal conductivity k_{SiC} (or k_{Si}) and heat capacity C_{SiC} (or C_{Si}) of the growth substrate. The heat capacities of the constituent layers are taken from the literature [31–35], which is a valid approach because the heat capacity varies little with material quality given fully dense material. The layer thicknesses are determined using cross-sectional transmission electron micrographs and scanning electron micrographs. We use bulk conductivity values for the Si and SiC substrates [29,30,36–39].

We quantify the sensitivity of the amplitude signal S_{α} to each of the parameters $\boldsymbol{\alpha}$ in the multilayer thermal model in a manner similar to those of Refs. [24,25]:

$$S_{\alpha} = \frac{\partial \ln\left(\sqrt{V_{\text{in}}{}^2 + V_{\text{out}}{}^2}\right)}{\partial \ln \boldsymbol{\alpha}}. \tag{1}$$

Figure 2 shows representative sensitivity plots for both GaN/AlN/SiC and GaN/AlN/Si composites at room temperature; the four sensitivities shown are the sensitivity to the Al/GaN thermal boundary resistance $R_{b,\text{Al-GaN}}$, to the GaN thermal conductivity k_{GaN}, to the effective AlN thermal resistance $R_{\text{AlN,eff}}$, and to the substrate thermal conductivity k_{SiC} (or k_{Si}). We normalize the amplitude signal by the signal at -100 ps (prepulse signal) to obtain the optimal sensitivity

to the buried GaN-substrate thermal interface. The sensitivity values are plotted as a function of the probe delay time and at a pump modulation frequency of 2 MHz. Best-fit values are assumed for each case. The sensitivities to $R_{b,\text{Al-GaN}}$ vary dynamically over most of the pump-probe delay time and are vastly different in curvature from those to k_{GaN} and $R_{\text{AlN,eff}}$. This allows us to isolate the Al/GaN thermal boundary resistance from the other two components (k_{GaN} and $R_{\text{AlN,eff}}$). The sensitivities to k_{GaN} and $R_{\text{AlN,eff}}$ are similar in shape over the entire range of delay time, and therefore the amplitude signal is influenced by a combination of the GaN conductivity and the AlN resistance. Variations in the substrate thermal conductivity become less important for the thickest GaN samples [see Figs. 2(b) and 2(d)] but are not negligible for the thinnest GaN samples [see Figs. 2(a) and 2(c)]. The substrate thermal conductivity also becomes less important with increasing temperature. For the worst case in the present experiment (i.e., 300 K), we estimate uncertainties in Si and SiC thermal conductivities as ±11% [29,30] and ±18% [36–39] from the literature values, respectively, which propagate into errors in $R_{\text{AlN,eff}}$ of ±12 and ±17%, respectively. We describe the propagation of errors in detail in the uncertainty analysis section (see Sec. II D).

We use the fact that the sensitivities to k_{GaN} and $R_{\text{AlN,eff}}$ vary with GaN thickness to determine both properties simultaneously. The absolute values of the sensitivity to k_{GaN} in the thickest GaN sample are approximately twice of those in the thinnest GaN sample over the entire delay time, whereas the absolute values of the sensitivity to $R_{\text{AlN,eff}}$ in the thickest GaN is less than half of those in the thinnest GaN. While we are simultaneously fitting three GaN thicknesses, the value of k_{GaN} is governed primarily by the thickest GaN sample whereas the value of $R_{\text{AlN,eff}}$ is mostly governed by the thinnest one under the assumption that these two properties do not vary strongly among the three samples [19].

There are two concerns here for our thickness-independent GaN conductivity assumption. The first is the size effect (i.e., the impact of boundary scattering, which depends on film thickness), and the second is the potential that samples with different thicknesses also have different defect densities. Estimates of the impact of phonon boundary scattering—using modifications to the semiclassical phonon conductivity integral (see Appendix A)—indicate that the relative errors in the GaN thermal conductivities are less than 12 and 7% at 300 and 550 K, respectively. The defect structures within a given thickness of the three films are almost certainly similar since all three samples were grown under identical growth conditions. Of greater concern is that the defect structure within the GaN layer might be nonhomogeneous due to near-interfacial disorder in the GaN: a high crystalline quality GaN region on top of a low-quality GaN region near the interface. Several transmission electron micrograph studies show that the low-quality GaN region can extend up to the first tens of nanometers from the GaN/AlN interface [5,8,9]. Since the low-quality GaN region is highly localized near the interface with the AlN, its resistance is indistinguishable from the GaN/AlN interface resistance (and thus the effective AlN resistance). Therefore, it is almost certain that the contribution from the low-quality GaN is included in the effective AlN resistance and that the defect structure within the GaN is homogenous. While this assumption—the homogeneous defect structure within the GaN layer—could overestimate the GaN conductivity, it is a reasonable first approximation and is consistent with the level of detail that the TDTR method can provide.

D. Uncertainty analysis

The uncertainties of the extracted thermal properties are analyzed through the standard error propagation analysis that has been widely employed in thermal property measurements using TDTR [25,40] and frequency-domain thermoreflectance [41]. The total uncertainty of the measurement of k_{GaN} and $R_{\text{AlN,eff}}$ comes from the propagation of errors of the input parameters $\boldsymbol{\alpha}_i$ in the multilayer thermal model, as defined by Eq. (2),

$$\Delta k_{\text{GaN}} = \sqrt{\sum_i \left(\frac{\partial k_{\text{GaN}}}{\partial \boldsymbol{\alpha}_i}\Delta\boldsymbol{\alpha}_i\right)^2},$$
$$\Delta R_{\text{AlN,eff}} = \sqrt{\sum_i \left(\frac{\partial R_{\text{AlN,eff}}}{\partial \boldsymbol{\alpha}_i}\Delta\boldsymbol{\alpha}_i\right)^2}, \quad (2)$$
$$\boldsymbol{\alpha}_i = d_{\text{Al}}, k_{\text{Al}}, C_{\text{Al}}, d_{\text{GaN}}, C_{\text{GaN}}, k_{\text{SiC}}\,(\text{or}\,k_{\text{Si}}), C_{\text{SiC}}\,(\text{or}\,C_{\text{Si}}).$$

The uncertainty in k_{GaN} (or $R_{\text{AlN,eff}}$) due to a single input parameter depends on the sensitivity $\partial k_{\text{GaN}}/\partial\boldsymbol{\alpha}_i$ (or $\partial R_{\text{AlN,eff}}/\partial\boldsymbol{\alpha}_i$) of k_{GaN} (or $R_{\text{AlN,eff}}$) to that parameter as well as on the uncertainty $\Delta\boldsymbol{\alpha}_i$ in that parameter [41]. In order to identify the sources of uncertainty in our measurement, we quantify the percent changes in k_{GaN} and $R_{\text{AlN,eff}}$ due to a 10% change in the specific input parameter $\boldsymbol{\alpha}_i$. Table I shows the resulting percent changes for the GaN/AlN/SiC composites at room temperature and indicates that the measurement of k_{GaN} and $R_{\text{AlN,eff}}$ is most sensitive to d_{Al} and C_{Al}, because the heat capacity per unit area of the Al film, $d_{\text{Al}}C_{\text{Al}}$, is the important parameter affecting the thermal response of the sample [40]. Since the heat capacity of the Al film should be close to the bulk value [40,42], the uncertainties in k_{GaN} and $R_{\text{AlN,eff}}$ are mostly determined by the uncertainty in the Al thickness. Uncertainty in the thermal conductivity of the growth substrate (SiC and Si) is another source of uncertainty, especially for $R_{\text{AlN,eff}}$, as can be inferred from Table I. Literature values for bulk Si thermal conductivity do not vary strongly: this variation is less than 11% from 148 W m^{-1} K^{-1} at room temperature [29,30]. On the other hand, SiC thermal conductivity values vary significantly in the literature—from 271 to 390 W m^{-1} K^{-1} at room temperature [36–39]. In our analysis, we account for this relatively large variation in the literature for SiC thermal conductivity. An independent laser flash measurement on the SiC substrate estimates that the SiC conductivity is

TABLE I. Percent changes in k_{GaN} and $R_{\text{AlN,eff}}$ due to a 10% change in the specific input parameter for GaN/AlN/SiC composites at $T = 300$ K. For example, a 10% change in the Al thickness d_{Al} results in 8.2% change in k_{GaN} and 14% change in $R_{\text{AlN,eff}}$.

	k_{Al}	d_{Al}	C_{Al}	d_{GaN}	C_{GaN}	k_{SiC}	C_{SiC}
Percent change in k_{GaN}	0.5	8.2	13.1	0.9	3.1	0.7	0.1
Percent change in $R_{\text{AlN,eff}}$	2.9	14.0	21.9	1.8	3.7	9.4	3.1

approximately 330 W m^{-1} K^{-1} at room temperature, which is within the reported range. These uncertainties of 11 and 18% in Si and SiC thermal conductivities propagate into errors in $R_{\mathrm{AlN,eff}}$ of 12 and 17%, respectively. With the uncertainties of C_{Al}, d_{Al}, C_{GaN}, and k_{SiC} being 2, 6, 2, and 18%, the overall uncertainties of k_{GaN} and $R_{\mathrm{AlN,eff}}$ for the GaN/AlN/SiC composites are 9 and 24%, respectively. For the GaN/AlN/Si composites, the corresponding uncertainties in k_{GaN} and $R_{\mathrm{AlN,eff}}$ are 11 and 16%, respectively.

III. RESULTS AND DISCUSSION

Both GaN/AlN/SiC and GaN/AlN/Si composites are measured for the temperature range of 300 to 550 K. We treat the GaN thermal conductivity k_{GaN}, the effective AlN thermal resistance $R_{\mathrm{AlN,eff}}$, and the Al/GaN thermal boundary resistances $R_{b,\mathrm{Al\text{-}GaN}}$ as adjustable parameters to simultaneously optimize the curve fits for all three GaN samples. We normalize the TDTR data at -100 ps (prepulse signal) to optimize the sensitivity to the buried GaN-substrate thermal interface (as discussed earlier) and fit the data over the full range of delay time, $-0.1 \leqslant t \leqslant 3.6$ ns. Representative TDTR traces and optimal analytical fits along with representative room-temperature values for each of the fitted variables are provided in Appendix A. The Al/GaN thermal boundary resistance ranges from 16 to 21 m^2 K GW^{-1} for the three GaN on SiC samples and from 6 to 18 m^2 K GW^{-1} for the three GaN on Si samples at room temperature. These variations are not atypical for lattice mismatched samples of this type and may result from varying concentrations of crystalline imperfections, as well as impurities and contamination effects, or from surface roughness in the atomic-scale near-interfacial region [19,27].

Figure 3 shows the extracted GaN thermal conductivities for both types of GaN composites as a function of temperature between 300 and 550 K. The thermal conductivities of GaN films decrease with rising temperature, which is characteristic of semiconducting materials in this temperature range due to the strong impact of phonon-phonon scattering. Here, we report a temperature dependence of $T^{-1.44}$ for GaN/AlN/SiC composites and $T^{-1.42}$ for GaN/AlN/Si composites. The GaN thermal conductivity values from past literature [43,44] are also shown in Fig. 3 for comparison with our data. Bulk GaN thermal conductivity data from Slack *et al.* [43] exhibit the temperature dependence $T^{-1.22}$, which is characteristic of pure adamantine crystal. The GaN conductivity values from Mion *et al.* [44] are slightly higher than our values, and their obtained temperature dependence of $T^{-1.43}$ is in reasonable agreement with the dependence observed in this study.

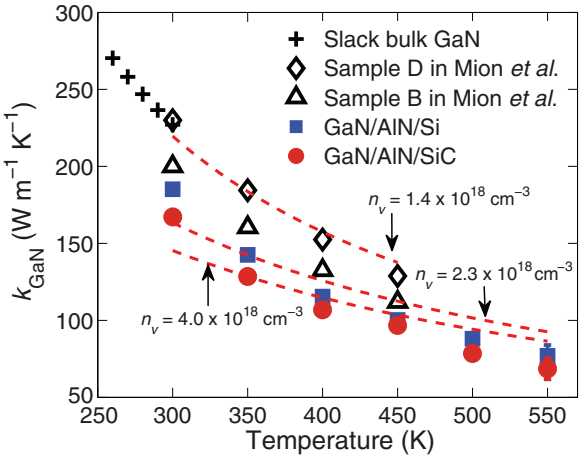

FIG. 3. (Color online) Temperature-dependent thermal conductivity of GaN film for our two GaN composites (solid squares and circles) and comparison with bulk GaN data from Slack *et al.* [43] (crosses) and from Mion *et al.* [44] (open diamonds and triangles). Modeled GaN thermal conductivities (red dashed lines) are also compared with the data at different vacancy concentration levels n_v. Overall uncertainties in the measured GaN thermal conductivity are ± 9 and ± 11% for GaN/AlN/SiC and GaN/AlN/Si composites, respectively.

To gain further physical insight into heat transport in GaN composites, we use the standard version of the semiclassical thermal conductivity integral [45], which can be adjusted to account for scattering on various types of imperfections. The relevant phonon scattering mechanisms in GaN films at our temperatures of interest include phonon-phonon Umklapp scattering, phonon-point defect scattering, phonon-dislocation scattering, and phonon-boundary scattering. Planar defects such as stacking faults are not considered here since these defects are barely seen in the electron micrographs in Figs. 1(a) and 1(b). This is in agreement with a past electron micrograph study [9], which revealed that the MOCVD-grown GaN/AlN/SiC composite is devoid of planar defects.

The Umklapp phonon scattering rate is modeled using [46,47]

$$\tau_U^{-1} = BT\omega^2 \exp\left(-\frac{C}{T}\right), \tag{3}$$

where B and C are adjustable parameters determined by fitting to data. Here, B is given by [46,47]

$$B = \frac{\hbar \gamma^2}{M v_s^2 \theta_D}, \tag{4}$$

where $\hbar$ is Plank's constant divided by 2π, γ is the Grüneisen parameter, M is the average mass of an atom in the crystal, v_s is the phonon group velocity, and θ_D is the Debye temperature. By fitting the model to the bulk GaN data by Slack *et al.* [43], we obtain $B = 1.82 \times 10^{-19}$ s K^{-1} and $C = 132$ K. Phonon scattering on point defects is typically treated using the Rayleigh model, where the scattering rate scales with the fourth power of the phonon frequency. High-frequency phonons are scattered more strongly by point defects than low-frequency phonons. In this treatment, the point defect scattering rate can be approximated using [48]

$$\frac{1}{\tau_P} = \frac{V_0 \Gamma \omega^4}{4\pi v_s^3}, \tag{5}$$

where V_0 is the unit volume for each atom and Γ represents the strength of the point defect scattering. Phonon scattering from dislocations includes the scattering either by the elastic strain field of the dislocation lines or by the cores of the dislocation lines [48]. The phonon scattering rate by the strain field of the dislocations scales linearly with the phonon frequency, and the scattering rate at the cores of the dislocations is proportional to the third power of the frequency [48]. Su *et al.*

[6] assumed in their model that the mean free path of phonons due to dislocations is limited to the average distance between dislocations (i.e., is independent of the phonon frequency). All of the above suggests that the dislocation scattering rate has weaker dependence on the phonon frequency than the point defect scattering rate. Since our work focuses on relatively high temperatures (up to 550 K), which approach the Debye temperature for GaN [46], the impact of high-frequency phonons on the reduction of the thermal conductivity is more significant than it is at cryogenic temperatures. This is especially true for heteroepitaxial GaN/AlN/SiC and GaN/AlN/Si structures since these materials are often highly defective and localized impurities and vacancies reduce thermal conductivity mainly at high frequencies. For high-frequency phonons, the impact of point defect scattering on the thermal conductivity reduction is postulated to be much stronger (due to its stronger frequency dependence) than that of dislocation scattering [49,50]. Thus, we mainly consider phonon scattering by point defects for simplicity. Also for simplicity, we consider only the vacancy as a type of point defect, since the vacancy is the strongest scatterer due to the large difference in mass between the vacancy and host. With these considerations, the strength of vacancy scattering can be written as [48]

$$\boldsymbol{\Gamma} = f_v \times [1 + 2 \times (6.4 \times \boldsymbol{\gamma})^2], \tag{6}$$

where f_v is the fractional concentration of vacancies and $\boldsymbol{\gamma}$ is the Grüneisen parameter to be determined from the fitted parameter B in Eq. (4). The total phonon scattering rate is determined by combining the relevant scattering rates through Matthiessen's rule.

Figure 3 plots the prediction of our thermal modeling with best-fit vacancy concentrations n_v for the data reported previously by Mion *et al.* [44], as well as the data reported here. While fitting for the vacancy concentration, we consider the boundary scattering with the scattering rate given by $\boldsymbol{\tau}_B^{-1} = v_s/L$, where L is the sample dimension. For the GaN data from Mion *et al.* [44], this is given by 370 and 2000 μm for sample B and D, respectively. For our GaN films, we consider the thickest film thicknesses for both cases, which are 1.6 and 1.7 μm for GaN/AlN/SiC and GaN/AlN/Si, respectively. The level of vacancy defects in GaN is consistent with the conductivity reductions observed in our GaN films. The modeled thermal conductivities decrease more slowly with temperature than the data collected, but they provide a plausible explanation for the strong temperature dependence. Residual impurities measured by Mion *et al.* [44] for one of their samples (open triangles in Fig. 3) are hydrogen (4×10^{17} cm^{-3}), carbon (10^{17} cm^{-3}), silicon (3×10^{16} cm^{-3}), and oxygen (10^{17} cm^{-3}). Another study [49] reported a Ga-vacancy concentration of 10^{18} cm^{-3} for GaN thermal conductivity in the range of 160 to 226 W m^{-1} K^{-1} at room temperature. These concentrations are comparable to our estimation of vacancy concentrations, although there is a slight difference due to the simplifications in our model. The vacancy concentrations obtained here could be extended to impurities by adjusting the mass difference in the strength of the point defect scattering $\boldsymbol{\Gamma}$ in Eq. (5). Different types of point defects affect only $\boldsymbol{\Gamma}$ and do not affect the overall temperature trend. Thus, although we do not account for detailed impurities, the shape of the modeled curve is correct.

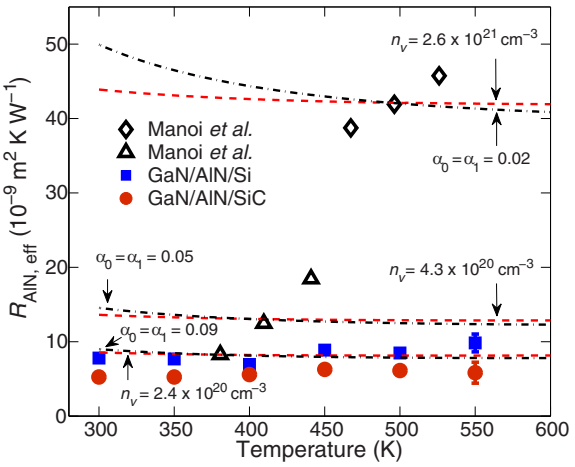

FIG. 4. (Color online) Temperature-dependent effective thermal resistance of the AlN film and its boundaries for GaN/AlN/SiC and GaN/AlN/Si composites (solid squares and circles). Modeled effective AlN resistances (red dashed lines) are compared with the data from Manoi *et al.* [17] (open diamonds and triangles), as well as our measured resistances for varying vacancy concentration levels n_v. The data from Manoi *et al.* [17] are the effective thermal resistances of 40-nm AlN transition films for their two GaN/AlN/SiC devices. For GaN/AlN/SiC, the transmission coefficients determined by DMM are 0.69 and 0.43 for the phonon transmission from the AlN into the GaN ($\boldsymbol{\alpha}_0$) and the SiC ($\boldsymbol{\alpha}_1$), respectively. The three black dashed-dotted lines represent the modeled effective AlN resistances obtained by purely fitting the data to the transmission coefficients (in the absence of vacancy defect scattering). Best-fit values of $\boldsymbol{\alpha}_0$ and $\boldsymbol{\alpha}_1$ are displayed for each case.

We find that the GaN thermal conductivity for the MBE-grown GaN/AlN/Si composites is slightly higher than that for the MOCVD-grown GaN/AlN/SiC composites. One possible explanation for this slightly higher thermal conductivity of the GaN on Si samples involves the difference in the growth method. The MBE growth method may offer advantages compared to the MOCVD method, including an ultrahigh vacuum growth environment, a low growth temperature, and the use of high-purity source materials, which could result in better material quality [51–54].

Figure 4 shows the effective thermal resistances of the AlN transition layers for both types of GaN composites at temperatures of 300–550 K. Overall, the effective AlN resistance in the Si-based composites is slightly higher than that in the SiC composites. This difference arises from a higher defect density in the Si-based composites due to the larger mismatch in thermal expansion coefficients and lattice parameters between GaN and Si when compared to the mismatch between GaN and SiC. A qualitative comparison of the electron micrographs in Fig. 1 also suggests that the AlN in the SiC composites has better crystalline quality and smoother GaN/AlN interface than that in the Si-based composites. The room-temperature AlN resistance for the SiC composites is consistent with that found in our previous study on GaN on SiC composites [19].

We perform simulations of the temperature-dependent effective resistance accounting for acoustic mismatch at the AlN interfaces and potential sources of phonon scattering

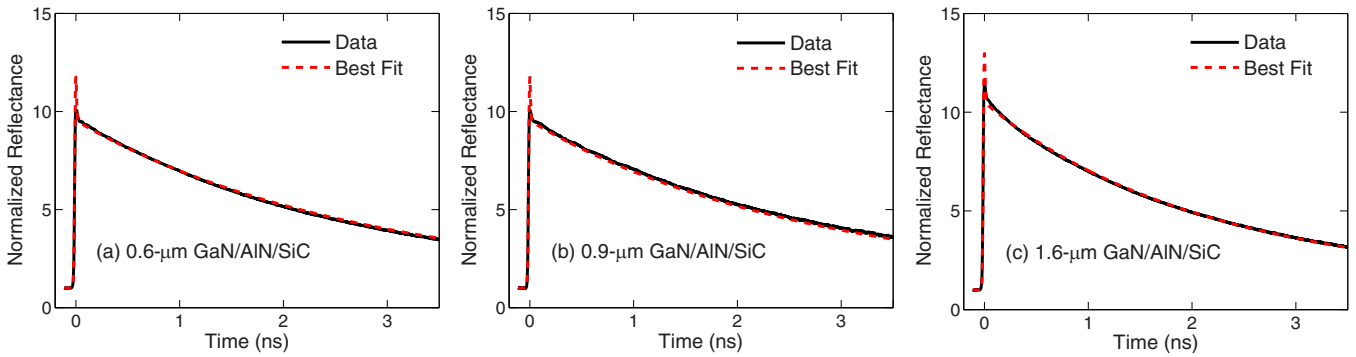

FIG. 5. (Color online) Representative TDTR data (solid line) and optimal analytical fits (dashed line) for (a) 0.6 μm GaN, (b) 0.9 μm GaN, and (c) 1.6 μm GaN on SiC composites at room temperature.

within the AlN volume. As in the GaN film analysis, the Umklapp phonon scattering parameters are adjusted to fit the model to the thermal conductivity data of defect-free AlN [55], yielding $B = 2.99 \times 10^{-19}$ s K^{-1} and $C = 380$ K. We, again, consider only the phonon-vacancy Rayleigh scattering as the type of defect scattering. We use an approximate solution to the phonon Boltzmann transport equation for the coupled effects of boundary and imperfection scattering in defective thin films. For a homogeneous film, this collapses to [12,56]

$$\frac{1}{R_{\mathrm{AlN,eff}}} = \frac{v_s}{3}\int_0^{\theta_D/T} \frac{C_V(x_\omega,T)}{\frac{d_{\mathrm{AlN}}}{v_s}\tau^{-1} + \frac{4}{3}\left(\frac{1}{\alpha_0}+\frac{1}{\alpha_1}-1\right)}dx_\omega, \quad (7)$$

where d_{AlN} is the AlN film thickness and $x_\omega = \hbar\omega/k_BT$ is the dimensionless phonon frequency. The phonon specific-heat function $C_V(x_\omega,T)$ is given in Ref. [56]. The diffuse mismatch model (DMM) [13,14] predicts the possibility of phonon transmission from within the AlN into the GaN and the substrate (SiC or Si), which are α_0 and α_1, respectively. Equation (7) is intended here as a more comprehensive model for the effective thermal resistance of a transition layer, which can serve as an effective thermal boundary resistance in practical simulations of much larger volumes [57].

In Fig. 4, the modeled effective thermal resistances of the AlN film at different concentrations of vacancies n_v are compared with past Raman data measured by Manoi *et al.* [17], as well as with our measured resistances. While our measured resistances remain below 10 m^2 K GW^{-1} with increasing temperature, the Raman data for 40-nm AlN films for their two GaN/AlN/SiC heterostructures have stronger temperature dependence than our data, and their measured values are substantially higher than our values. Another Raman study [18] reported 33 m^2 K GW^{-1} at 573 K as an effective AlN resistance for a GaN/AlN/Si heterostructure, which is also considerably higher than our values for the Si-based composites. The lower resistances observed here are due to a lower defect density in the AlN transition layer, as indicated by the level of vacancy defects in our model. If we use the vacancy concentration in the AlN layer as an adjustable parameter to fit the model to our data, the best-fit vacancy concentrations are about 2.4×10^{20} cm^{-3} and 1.1×10^{20} cm^{-3} for GaN/AlN/Si and GaN/AlN/SiC composites, respectively. The agreement between our data and the model is relatively good, but a discrepancy exists between the Raman data and the model. The exact cause of this discrepancy is not yet understood. The modeled effective AlN resistances with dislocation scattering [6] (instead of vacancy scattering) considered deviate more from the data and do not capture the temperature trend properly, especially when the AlN resistance is high (not shown in Fig. 4 for brevity). The best-fit dislocation densities ($\rho_D = 10^{13}-10^{15}$ cm^{-2}) for the data are also too high, compared to dislocation densities ($\rho_D = 10^{10}-10^{12}$ cm^{-2}) reported by past electron micrograph studies [5–7]. These findings support our hypothesis that point defect scattering rather than dislocation scattering dominates the temperature trend of the AlN resistance.

Here, we document a further effort to understand the temperature trend of the effective AlN resistance. In this case we investigate the possibility that the data could be accommodated without vacancy or dislocation scattering by simply adjusting the two transmission coefficients (α_0 and α_1). Such model predictions (three black dashed-dotted lines) are shown in Fig. 4, with best-fit transmission coefficients for the data by Manoi *et al.* [17], as well as our data. The fitted transmission coefficients decrease with increasing resistance, and significantly lower values (0.02 to 0.09) are required to match the AlN data compared to those based on the DMM. For instance, the transmission coefficients determined by DMM are 0.69 and 0.43 for the phonon transmission from the AlN into the GaN (α_0) and the SiC (α_1), respectively. This approach can lead to the opposite temperature trend compared to the data, especially when the resistance is high (see the top-most black dashed-dotted line and open diamonds

TABLE II. Extracted thermal properties of three GaN/AlN/SiC composites at $T = 300$ K.

Sample	$R_{b,\,\mathrm{Al\text{-}GaN}}$ (m^2 K GW^{-1})	k_{GaN} (W m^{-1} K^{-1})	$R_{\mathrm{AlN,\,eff}}$ (m^2 K GW^{-1})
0.6 μm GaN/AlN/SiC	21.2 ± 1.4	–	–
0.9 μm GaN/AlN/SiC	20.8 ± 1.5	167 ± 15	5.3 ± 1.3
1.6 μm GaN/AlN/SiC	16.1 ± 1.2	–	–

TABLE III. Extracted thermal properties of three GaN/AlN/Si composites at $T = 300$ K.

Sample	$R_{b,\,\text{Al-GaN}}$ (m^2 K GW^{-1})	k_{GaN} (W m^{-1} K^{-1})	$R_{\text{AlN,\,eff}}$ (m^2 K GW^{-1})
0.5 μm GaN/AlN/Si	6.2 ± 0.4	–	–
1.3 μm GaN/AlN/Si	11.7 ± 0.9	185 ± 20	7.8 ± 1.2
1.7 μm GaN/AlN/Si	17.6 ± 1.4	–	–

in Fig. 4). However, when the resistance is low, this approach is consistent with the magnitude and trend of the data, similar to the model considering vacancy defect scattering in the AlN with the transmission coefficients determined by the DMM (see the bottom-most black dashed-dotted and red dashed lines in Fig. 4). Although the transmission coefficients do not directly account for defects on either side of the medium, the fact that the model requires considerably lower values than those predicted by the DMM may suggest the potential role played by near-interfacial defects around the AlN interfaces with the adjacent GaN and substrate. A recent transmission electron micrograph [58] (not of our samples but relevant) illustrated planar defects within a few nanometers of the AlN interface with the rough SiC, which further supports the potential importance of near-interfacial defects. As a consequence, a combination of near-interfacial defects and point defects within the AlN transition film may be responsible for the AlN resistance, rather than only defects in the AlN.

IV. CONCLUSIONS

This work extracts the GaN thermal conductivities and the effective thermal resistances of the AlN transition layers simultaneously for two types of GaN composites using TDTR at temperatures relevant to the operation of power transistor devices. An approximate solution to the phonon Boltzmann transport equation is used to present a comprehensive model for the effective resistance of the AlN film, which accounts for the combined effects of boundary and imperfection scattering. The trend with increasing temperature is consistent with vacancy concentrations on the order of 10^{18} cm^{-3} for the GaN and 10^{20} cm^{-3} for the AlN. The model with only the transmission coefficients adjusted (without considering point defect scattering in the AlN) is also in reasonable agreement with the measured AlN resistances. Our findings indicate that a combination of point defects within the AlN transition layer and near-interfacial defects may be responsible for the thermal conduction resistance of the AlN transition layer.

ACKNOWLEDGMENTS

The authors acknowledge financial support from the Air Force Office of Scientific Research (Grant No. FA9550-12-1-0195, titled "MultiCarrier and low-dimensional thermal conduction at interfaces for high power electronic devices") and the Defense Advanced Research Projects Agency Microsystems Technology Office through the Air Force (Grant No. FA8650-10-1-7044, titled "Device-level thermal management for HEMT radar: thermal metrology, interfaces, and metrics"). The work of J.C. was supported in part by a Samsung scholarship.

APPENDIX A: ADDITIONAL DETAILS OF TDTR DATA ANALYSIS

Figure 5 shows representative thermal traces with the optimal analytical fits at room temperature for three GaN on SiC samples. The thermal traces are normalized at -100 ps (prepulse signal) to maximize the sensitivity to the buried GaN-substrate thermal interface, as discussed in the main text. A nonlinear least-squares curve-fitting algorithm finds

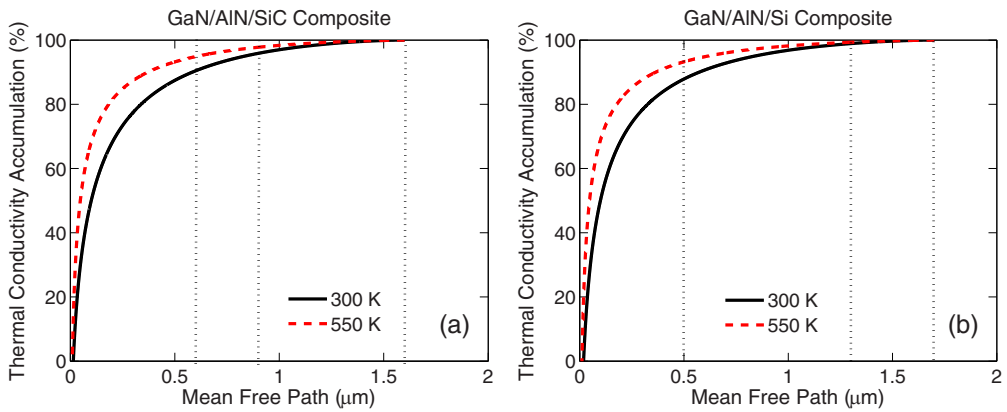

FIG. 6. (Color online) Thermal conductivity (cross-plane) accumulation with phonon mean free path for GaN films of (a) GaN/AlN/SiC and (b) GaN/AlN/Si composites, calculated using the thermal conductivity integral model from Callaway [45], with the Umklapp and vacancy scattering parameters as specified in the main text. Black solid lines represent the thermal conductivity accumulation at room temperature, and red dashed lines represent the accumulation at $T = 550$ K. The vertical black dotted lines represent the GaN thicknesses.

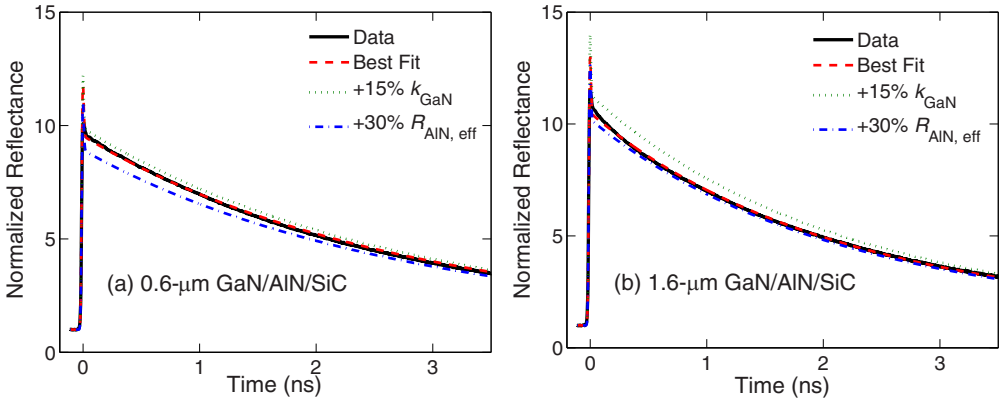

FIG. 7. (Color online) Sensitivity of TDTR measurement to k_{GaN} and $R_{AlN,eff}$ for (a) the thinnest GaN/AlN/SiC and (b) the thickest GaN/AlN/SiC at room temperature. The black solid lines are the data for the two samples, and the red dashed lines represent the best-fit curves with $k_{GaN} = 167$ W m^{-1} K^{-1} and $R_{AlN,eff} = 5.3$ m^2 K GW^{-1}. The green dotted and blue dashed-dotted curves illustrate the analytical fits obtained by varying best-fit k_{GaN} by +15% and $R_{AlN,eff}$ by +30%, respectively. The thinnest GaN sample has the best sensitivity to $R_{AlN,eff}$ and the least sensitivity to k_{GaN}. The thickest GaN sample is most sensitive to k_{GaN} and least sensitive to $R_{AlN,eff}$.

the Al/GaN thermal boundary resistances, the GaN thermal conductivity, and the effective AlN thermal resistance that simultaneously optimize the curve fits for all three samples. Representative room-temperature values for the extracted variables are provided in Tables II and III for both GaN/AlN/SiC and GaN/AlN/Si composites.

Our strategy is to use multiple samples with varying GaN thicknesses from the same fabrication process to extract the Al/GaN thermal boundary resistance, the GaN thermal conductivity, and the effective AlN thermal resistance simultaneously with reasonably low uncertainty. The key assumption here is that GaN thermal conductivities do not vary strongly among the samples [19]. One of the major issues here is the size effect, the impact of boundary scattering, which depends on film thickness. To support our argument that the difference between GaN thermal conductivities of different thickness samples is small for our thickness range, we quantify the contribution of ballistic phonons in our GaN films, employing the semiclassical thermal conductivity integral model [45] with Umklapp and vacancy scattering. The Umklapp scattering parameters and fitted vacancy concentrations are described in the main text. Diffuse phonon scattering at film boundaries (we take the thickest film thicknesses for both composites, which are 1.6 and 1.7 μm for GaN/AlN/SiC and GaN/AlN/Si, respectively) is also considered in calculating the total scattering rate. Figure 6 plots the accumulation of thermal conductivity as a function of the phonon mean free path for both GaN/AlN/SiC and GaN/AlN/Si at two representative temperatures (300 and 550 K). For the GaN/AlN/SiC, about 90% of the total thermal conductivity is contributed by phonons with mean free paths smaller than the thinnest GaN thickness (0.6 μm) at 300 K, while this contribution is about 95% at 550 K. This could lead to 10 and 5% differences in GaN thermal conductivity between the thinnest and thickest GaN on SiC samples at 300 and 550 K, respectively. For the GaN/AlN/Si, this difference is 12 and 7% at 300 and 550 K, respectively.

We think that the impact of such size effects on the actual fitted conductivities is minimal even for the worst-case scenario (room-temperature data). Representative sensitivity analysis in the main text shows that the GaN thermal conductivity is mostly determined by the thickest sample and not much affected by the thinnest sample. To further support this argument, we plot the TDTR data along with the optimal analytical fits for the thinnest and thickest GaN on SiC samples and illustrate the parameter extraction sensitivity by varying one parameter from its optimal value in Fig. 7. Clearly, the GaN thermal conductivity has a much stronger impact on the thermal trace of the thickest sample [see Fig. 7(b)] than on that of the thinnest one, for which it has a minimal impact [see Fig. 7(a)]. On the other hand, the effective AlN thermal resistance has a much stronger impact on the thermal trace of the thinnest sample than on that of the thickest one, for which its impact is minimal. Therefore, the thermal conductivity reduction estimated above in the thinnest GaN sample is less important and the impact of the size effect is not significant in our data-fitting approach.

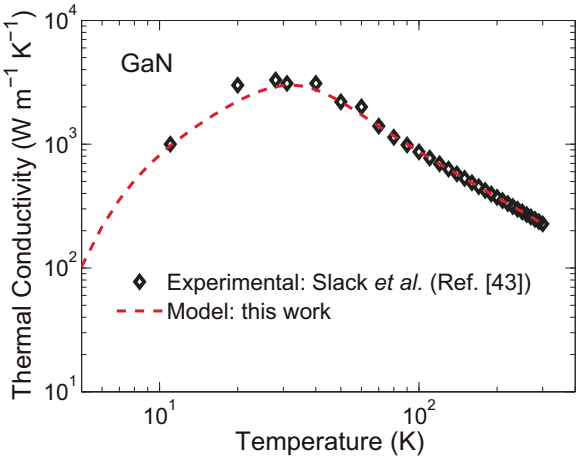

FIG. 8. (Color online) Comparison of the modeled GaN thermal conductivity with the experimental bulk GaN data (Slack *et al.* [43]). The comparison suggests that the model can account well for both the magnitude and the temperature dependence of the bulk GaN thermal conductivity.

APPENDIX B: THERMAL CONDUCTIVITY MODEL FIT TO BULK CONDUCTIVITY DATA

As explained in the main text, we determine the Umklapp scattering parameters [B and C in Eq. (3)] by fitting the thermal conductivity model to the bulk conductivity data (the data for GaN and AlN are from Refs. [43] and [55], respectively). The bulk GaN data from Slack *et al*. [43] are for a high-purity single crystal, as evidenced by their observed temperature dependence $T^{-1.22}$ from 80 to 300 K, which is characteristic of pure adamantine crystals. Thus, we do not consider phonon scattering by other impurities (except phonon-isotope scattering) for their GaN data. Similarly, since we use the data of defect-free AlN from Slack *et al*. [55], we also do not consider other impurities except isotopes for their AlN data. While identifying the Umklapp scattering parameters for GaN and AlN, we use the isotope scattering strength Γ of 2.74×10^{-4} [46] for GaN and 4.29×10^{-6} [59] for AlN and use the sample dimension of 500 μm [43] for GaN and 0.54 cm [55] for AlN. The Debye temperatures for GaN and AlN are calculated in a manner similar to that used in Ref. [60]. As an example, we plot our GaN thermal conductivity model with the bulk GaN data by Slack *et al*. [43] in Fig. 8.

[1] S. Nakamura, M. Senoh, S. Nagahama, N. Iwasa, T. Yamada, T. Matsushita, H. Kiyoku, and Y. Sugimoto, Jpn. J. Appl. Phys. **35**, L74 (1996).
[2] S. Nakamura, M. Senoh, N. Isawa, and S. Nagahama, Appl. Phys. Lett. **67**, 1868 (1995).
[3] U. K. Mishra, P. Parikh, and Y.-F. Wu, Proc. IEEE **90**, 1022 (2002).
[4] E. Cho, Ph.D. thesis, University of Michigan, 2009.
[5] Z. J. Reitmeier, S. Einfeldt, R. F. Davis, X. Zhang, X. Fang, and S. Mahajan, Acta Mater. **57**, 4001 (2009).
[6] Z. Su, L. Huang, F. Liu, J. P. Freedman, L. M. Porter, R. F. Davis, and J. A. Malen, Appl. Phys. Lett. **100**, 201106 (2012).
[7] V. M. Torres, M. Stevens, J. L. Edwards, D. J. Smith, R. B. Doak, and I. S. T. Tsong, Appl. Phys. Lett. **71**, 1365 (1997).
[8] E. Cho, A. Mogilatenko, F. Brunner, E. Richter, and M. Weyers, J. Cryst. Growth **371**, 45 (2013).
[9] N. Faleev and I. Levin, J. Appl. Phys. **107**, 113529 (2010).
[10] A. Majumdar, J. Heat Transfer **115**, 7 (1993).
[11] G. Chen and C. L. Tien, J. Thermophys. Heat Transfer **7**, 311 (1993).
[12] K. E. Goodson, J. Heat Transfer **118**, 279 (1996).
[13] E. T. Swartz and R. O. Pohl, Rev. Mod. Phys. **61**, 605 (1989).
[14] L. De Bellis, P. E. Phelan, and R. S. Prasher, J. Thermophys. Heat Transfer **14**, 144 (2000).
[15] R. M. Costescu, M. A. Wall, and D. G. Cahill, Phys. Rev. B **67**, 054302 (2003).
[16] P. G. Klemens, Phys. Rev. **119**, 507 (1960).
[17] A. Manoi, J. W. Pomeroy, N. Killat, and M. Kuball, IEEE Electron Device Lett. **31**, 1395 (2010).
[18] A. Sarua, H. Ji, K. P. Hilton, D. J. Wallis, M. J. Uren, T. Martin, and M. Kuball, IEEE Trans. Electron Devices **54**, 3152 (2007).
[19] J. Cho, E. Bozorg-Grayeli, D. H. Altman, M. Asheghi, and K. E. Goodson, IEEE Electron Device Lett. **33**, 378 (2012).
[20] J. Kuzmik, S. Bychikhin, D. Pogany, C. Gaquiere, E. Pichonat, and E. Morvan, J. Appl. Phys. **101**, 054508 (2007).
[21] W. S. Capinski and H. J. Maris, Rev. Sci. Instrum. **67**, 2720 (1996).
[22] D. G. Cahill, Rev. Sci. Instrum. **75**, 5119 (2004).
[23] H.-K. Lyeo and D. G. Cahill, Phys. Rev. B **73**, 144301 (2006).
[24] A. J. Schmidt, X. Chen, and G. Chen, Rev. Sci. Instrum. **79**, 114902 (2008).
[25] Y. K. Koh, S. L. Singer, W. Kim, J. M. O. Zide, H. Lu, D. G. Cahill, A. Majumdar, and A. C. Gossard, J. Appl. Phys. **105**, 054303 (2009).
[26] M. A. Panzer, Ph.D. thesis, Stanford University, 2010.
[27] J. P. Reifenberg, K. W. Chang, M. Panzer, S. B. Kim, J. A. Rowlette, M. Asheghi, H. S. P. Wong, and K. E. Goodson, IEEE Electron Device Lett. **31**, 56 (2010).
[28] D. G. Cahill, Rev. Sci. Instrum. **61**, 802 (1990).
[29] C. Y. Ho, R. W. Powell, and P. E. Liley, J. Phys. Chem. Ref. Data **1**, 279 (1972).
[30] S.-M. Lee and D. G. Cahill, J. Appl. Phys. **81**, 2590 (1997).
[31] W. F. Giauque and P. F. Meads, J. Am. Chem. Soc. **63**, 1897 (1941).
[32] I. Zięborak-Tomaszkiewicz, E. Utzig, and P. Gierycz, J. Thermal Anal. Calorim. **91**, 329 (2008).
[33] B. A. Danilchenko, T. Paszkiewicz, S. Wolski, A. Jezowski, and T. Plackowski, Appl. Phys. Lett. **89**, 061901 (2006).
[34] L. Hitova, R. Yakimova, E. P. Trifonova, A. Lenchev, and E. Janzen, J. Electrochem. Soc. **147**, 3546 (2000).
[35] P. Flubacher, A. J. Leadbetter, and J. A. Morrison, Philos. Mag. **4**, 273 (1959).
[36] E. A. Burgemeister, W. von Münch, and E. Pettenpaul, J. Appl. Phys. **50**, 5790 (1979).
[37] P. Wutimakun, H. Miyazaki, Y. Okamoto, J. Morimoto, T. Hayashi, and H. Shiomi, Mater. Sci. Forum **600**, 521 (2009).
[38] G. P. Su, X. H. Zheng, L. Qiu, D. W. Tang, and J. Zhu, Int. J. Thermophys. **34**, 2334 (2013).
[39] R. Wei, S. Song, K. Yang, Y. Cui, Y. Peng, X. Chen, X. Hu, and X. Xu, J. Appl. Phys. **113**, 053503 (2013).
[40] C. Wei, X. Zheng, D. G. Cahill, and J.-C. Zhao, Rev. Sci. Instrum. **84**, 071301 (2013).
[41] J. A. Malen, K. Baheti, T. Tong, Y. Zhao, J. A. Hudgings, and A. Majumdar, J. Heat Transfer **133**, 081601 (2011).
[42] D. R. Queen and F. Hellman, Rev. Sci. Instrum. **80**, 063901 (2009).
[43] G. A. Slack, L. J. Schowalter, D. Morelli, and J. A. Freitas, Jr., J. Cryst. Growth **246**, 287 (2002).
[44] C. Mion, J. F. Muth, E. A. Preble, and D. Hanser, Appl. Phys. Lett. **89**, 092123 (2006).
[45] J. Callaway, Phys. Rev. **113**, 1046 (1959).
[46] D. T. Morelli, J. P. Heremans, and G. A. Slack, Phys. Rev. B **66**, 195304 (2002).
[47] W. Liu and A. A. Balandin, J. Appl. Phys. **97**, 073710 (2005).
[48] J. Zou, D. Kotchetkov, A. A. Balandin, D. I. Florescu, and F. H. Pollak, J. Appl. Phys. **92**, 2534 (2002).

[49] A. Jezowski, B. A. Danilchenko, M. Bockowski, I. Grzegory, S. Krukowski, T. Suski, and T. Paszkiewicz, Solid State Commun. **128**, 69 (2003).
[50] A. AlShaikhi, S. Barman, and G. P. Srivastava, Phys. Rev. B **81**, 195320 (2010).
[51] J. Z. Li, J. Y. Lin, H. X. Jiang, A. Salvador, A. Votchkarev, and H. Morkoc, Appl. Phys. Lett. **69**, 1474 (1996).
[52] S. C. Jain, M. Willander, J. Narayan, and R. V. Overstraeten, J. Appl. Phys. **87**, 965 (2000).
[53] H. Xing, S. Keller, Y.-F. Wu, L. McCarthy, I. P. Smorchkova, D. Buttari, R. Coffie, D. S. Green, G. Parish, S. Heikman, L. Shen, N. Zhang, J. J. Xu, B. P. Keller, S. P. DenBaars, and U. K. Mishra, J. Phys.: Condens. Matter **13**, 7139 (2001).
[54] Y. Huo, Ph.D. thesis, Stanford University, 2010.
[55] G. A. Slack, R. A. Tanzilli, R. O. Pohl, and J. W. Vandersande, J. Phys. Chem. Solids **48**, 641 (1987).
[56] K. E. Goodson, O. W. Kaeding, M. Roesler, and R. Zachai, J. Appl. Phys. **77**, 1385 (1995).
[57] J. Cho, Z. Li, M. Asheghi, and K. E. Goodson, Annu. Rev. Heat Transfer (to be published).
[58] Z. Su, J. P. Freedman, J. H. Leach, E. A. Preble, R. F. Davis, and J. A. Malen, J. Appl. Phys. **113**, 213502 (2013).
[59] Y. K. Koh, Y. Cao, D. G. Cahill, and D. Jena, Adv. Funct. Mater. **19**, 610 (2009).
[60] R. Cheaito, J. C. Duda, T. E. Beechem, K. Hattar, J. F. Ihlefeld, D. L. Medlin, M. A. Rodriguez, M. J. Campion, E. S. Piekos, and P. E. Hopkins, Phys. Rev. Lett. **109**, 195901 (2012).